

Microwave response of NbSe₂ van der Waals Josephson junctions

Shixian Chen,^{1,*} Wanghao Tian,^{1,*} Zuyu Xu,¹ Ping Zhang,¹ Hongmei Du,¹ Zihan Wei,¹ Dingding Li,¹ Yangyang Lv,¹ Hancong Sun,² Yong-Lei Wang,¹ Dieter Koelle[Ⓞ],³ Reinhold Kleiner,^{3,†} Huabing Wang[Ⓞ],^{1,2,‡} and Peiheng Wu^{1,2}

¹Research Institute of Superconductor Electronics, Nanjing University, Nanjing 210023, China

²Purple Mountain Laboratories, Nanjing 211111, China

³Physikalisches Institut, Center for Quantum Science and LISA⁺, Universität Tübingen, D-72076 Tübingen, Germany



(Received 23 June 2021; revised 27 October 2021; accepted 8 December 2021; published 27 December 2021)

van der Waals Josephson junctions utilize the interface between two superconducting NbSe₂ crystal flakes as a tunnel barrier. We fabricate such junctions by a dry-transfer procedure and characterize them by electric transport experiments at various temperatures and under microwave irradiation at frequencies up to 224 GHz. We observe integer Shapiro steps in the current-voltage characteristics indicating a sinusoidal Josephson current-phase relation and the possibility to use this kind of junction even in the terahertz frequency range.

DOI: [10.1103/PhysRevB.104.214512](https://doi.org/10.1103/PhysRevB.104.214512)

I. INTRODUCTION

Josephson junctions are the key elements of superconducting circuits and find applications in microwave and terahertz signal detection [1,2], photon detection in quantum computing [3,4], dark-matter axion search [5], and many other fields. During the last decades, electronic devices based on two-dimensional (2D) materials attracted great interest [6–12]. NbSe₂, a transition-metal dichalcogenide crystallizing in a van der Waals (vdW) layer structure [13–15], undergoes a phase transition from its metallic state to the superconducting state below about 7 K for thick samples and at a somewhat reduced critical temperature for few-layer NbSe₂ [16–18]. NbSe₂ Josephson junctions were formed by using graphene as a barrier layer [19,20] and, recently, Josephson junctions and even superconducting quantum interference devices formed between two NbSe₂ flakes have been reported, where the vdW gap at the interface between the two superconducting flakes acts as a tunneling barrier [21,22]. A dry-transfer and mechanical stacking technology are typically used to place the NbSe₂ flakes on top of each other to form the junction.

While the DC Josephson effect and quantum interference has been clearly demonstrated for NbSe₂ vdW Josephson junctions, there seems to be a lack of investigations of the ac Josephson effect, which is utilized in many of the applications of Josephson junctions. This motivates our study which focuses on the behavior of such junctions in microwave fields with frequency f up to 224 GHz. We characterize the junctions in transport experiments, recording and analyzing current-voltage characteristics (IVCs) at different temperatures. In microwave fields pronounced Shapiro steps are observed, indicating that the NbSe₂ vdW Josephson junctions

are in principle suited for electronic applications even at terahertz frequencies.

II. SAMPLE FABRICATION AND MEASUREMENT TECHNIQUES

In the fabrication process, like in the one described in Ref. [22], we first pattern the electrodes contacting the NbSe₂ flakes. To do so, photoresist is coated on a sapphire substrate and patterned with a laser writer. A 5-nm-thick Ti film and then a 30-nm-thick Au film are deposited *in situ* by DC magnetron sputtering. After lifting off the films on the resist with acetone, the electrodes needed for electrical transport measurements are formed. To obtain the NbSe₂ flakes, in a first step a piece of polydimethylsiloxane (PDMS) is attached to a glass slide, and with the help of scotch tape and PDMS several NbSe₂ flakes are obtained by repeated peeling of a bulk NbSe₂ crystal. To position suitable NbSe₂ flakes on the preprepared electrodes we use a dry-transfer setup integrated in a microscope. The setup contains an adjustable holder for the glass slide and a holder to place the substrate. The glass slide with the NbSe₂ flakes is mounted in the dry-transfer setup and the relative position between the PDMS and the substrate is adjusted so that a NbSe₂ flake is above the preprepared electrodes. Then the glass slide is lowered until the NbSe₂ flake is in contact with the substrate. Next, the substrate is heated to 70 °C for 1 min to weaken the adhesion between the NbSe₂ flakes and the PDMS. Subsequently, the glass slide is slowly lifted, leaving all NbSe₂ flakes on the substrate. Having prepared the bottom NbSe₂ superconducting electrode this way, the process is repeated to position the NbSe₂ flake forming the top superconducting electrode. The overlap area of two superconducting NbSe₂ electrodes, i.e., the vdW Josephson junction area, can be defined by adjusting the relative position between the top and bottom NbSe₂ flakes. Note that the interfaces between the Au electrodes and NbSe₂, and between the two NbSe₂ flakes, never touch any chemical solvents in the entire fabrication process. The freshly cleaved

*These authors contributed equally to this work.

†kleiner@uni-tuebingen.de

‡hbwang@nju.edu.cn

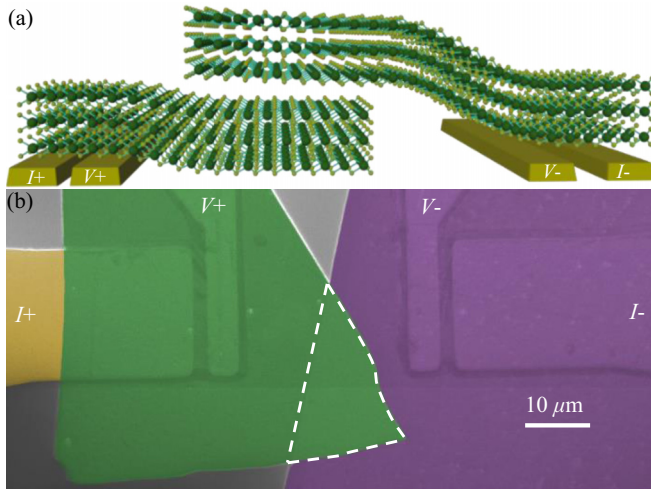


FIG. 1. (a) Schematic drawing of the vdW Josephson junction. (b) False-color scanning electron microscope image of junction A. Current and voltage terminals are indicated. The white dashed line indicates the junction area.

NbSe₂ single crystal is exposed to the atmosphere for only a few minutes; thus, the interface deterioration can be minimized. The contact resistance between the NbSe₂ and the Au electrode is $\sim 10 \Omega$, with a typical overlap area of $\sim 400 \mu\text{m}^2$.

In this paper we focus on two samples referred to as junction A and junction B. For junction A the thickness of the bottom NbSe₂ flakes is about 50 nm and for the top flake it is about 30 nm. For junction B the thicknesses are 100 and 130 nm, respectively. The junction areas are 100 and 175 μm^2 for junctions A and B, respectively. A schematic of the vdW Josephson junction and a scanning electron microscope image of junction A are shown in Fig. 1. The white dashed line indicates the overlap region of two NbSe₂ flakes, i.e., the junction area. Also, the current and voltage terminals are indicated.

The electric transport properties of the two samples were measured in a Gifford-McMahon type refrigerator for temperatures down to 2.95 K, using a standard four-terminal configuration.

For microwave irradiation, frequencies below 40 GHz are generated by a frequency generator and transported by a coaxial line with an antenna at the terminal about 1 cm height above the sample. For higher frequencies above 100 GHz we use a Virginia Diodes Inc. source to generate the microwave and radiate the microwave onto the sample through a window which is transparent for terahertz radiation.

We also note that, despite our efforts to minimize surface degradation of the NbSe₂ flakes, we observed a strong sample-to-sample variation. In total we fabricated nine junctions. Current-voltage characteristics of the junctions not discussed in the main paper and a table with selected electrical and geometrical parameters are shown in Appendix A. Out of the seven junctions not further discussed in this paper, two showed clear signatures of overheating, with strongly hysteretic IVCs and voltages exceeding 20 mV in the resistive state. Four junctions had nonhysteretic IVCs, partially with a large excess current. One junction had a tunneling-like IVC but with a highly suppressed critical current. This strong

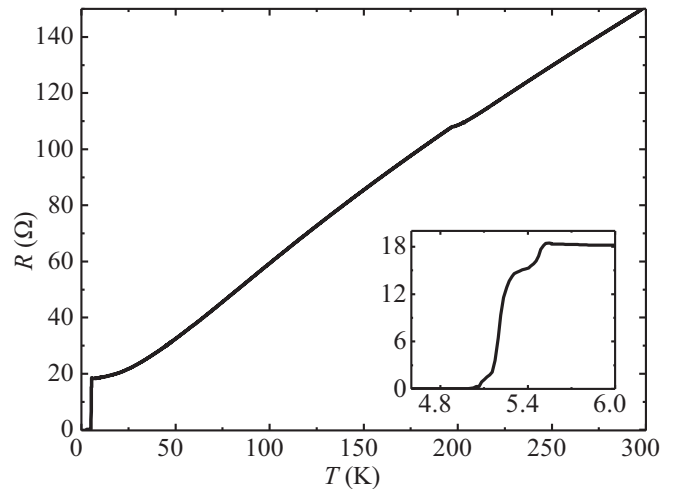


FIG. 2. Resistance R across junction A vs temperature (recorded with a bias current $I = 10 \mu\text{A}$). The inset shows the resistive transition of junction A on an enlarged scale.

variation may be caused by some shunts by currents flowing in plane rather than through the vertical vdW contact area. Also, the relative orientation of the crystal axes of the two flakes—which we did not control in our experiments—may play a role, as it has been noted in Ref. [22]. Additional inhomogeneities may arise from PDMS contamination of the vdW interface. We could see only a few contaminations on the surface of NbSe₂ under the optical microscope. Such “macroscopic” polymer contaminations should mainly result in some insulating regions in the vdW interface, reducing the effective junction area. Atomic-scale Si-based contaminants may indeed alter the interface tunnel barrier, but it is unlikely that they lead to the overheating or shunting effects we observe in several junctions.

Given the fact that we have a strong scatter in the properties of our junctions we find it important to show a complete set of data for more than one junction. Junction A and junction B are similar in the sense that they both have a tunneling-like hysteretic IVC. As we will show, both junctions have a very similar capacitance per area. We estimate the distance between the two NbSe₂ flakes to be 0.75 nm, which is close to the vdW gap in pristine single crystals (0.6 nm). Still, the two junctions differ by one order of magnitude in their critical current density and by a factor of 4 in their resistance-area product. These differences cause, for example, a different susceptibility to heating effects. In terms of microwave irradiation they allow us to investigate the ac Josephson effect in very different parameter regimes.

III. RESULTS

A. DC characterization

Figure 2 shows the resistance R versus temperature T curve of junction A from room temperature to 2.95 K, with a bias current I of 10 μA . The resistance sharply decreases below 5.5 K and finally vanishes at about 5 K, corresponding to the superconducting transition of NbSe₂ flakes. A small foot structure is visible at the bottom of the $R(T)$ curve, which

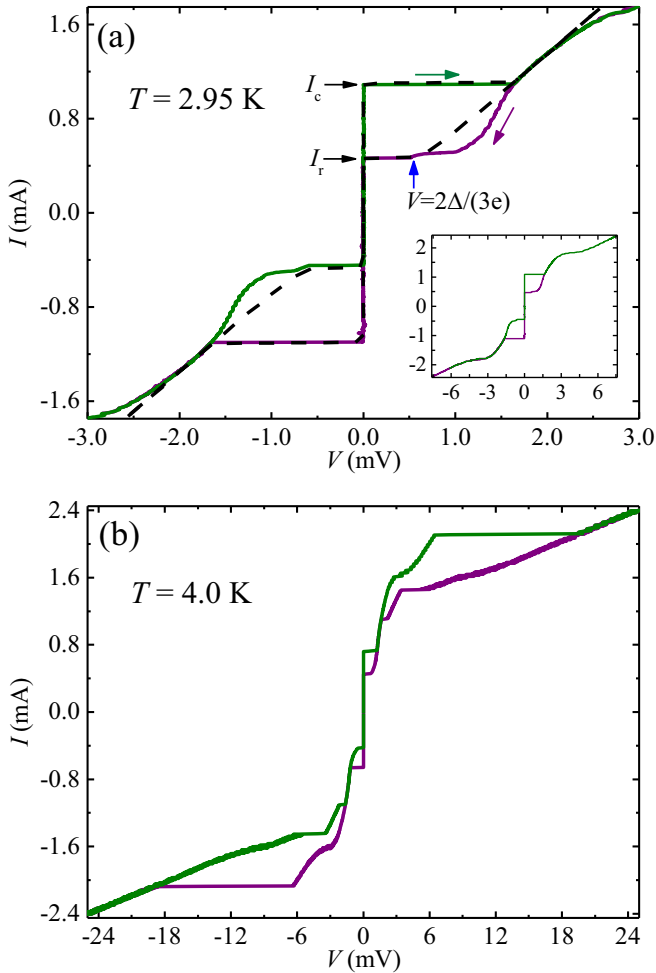


FIG. 3. (a) IVC of junction A at a bath temperature of 2.95 K. Current sweep directions are indicated by the arrows and the color of the symbols. The vertical arrow indicates the subgap feature near $2\Delta/3e$. The inset shows the IVC on a larger voltage scale. The dashed line indicates a simulated IVC based on the RCSJ model. (b) IVC of junction A at a bath temperature of 4.0 K.

indicates that the critical current of the junction is below the bias current. Further note that the T_c of the NbSe₂ flakes is about 2 K lower than the 7 K expected for bulk samples and also 30–50-nm-thick flakes. The degradation of the crystals presumably occurred during the 5-y storage time of the crystals in a dry atmosphere.

In Fig. 3(a) we display the IVC of junction A at a bath temperature of 2.95 K. The olive line in Fig. 3(a) is for the current sweep from negative to positive current and the purple line for the current sweep from positive to negative current. When the bias current reaches the critical current $I_c \approx 1.1$ mA, the voltage jumps to a value of about 1.64 mV. Above the critical current the differential resistance initially increases slightly with increasing bias current and more rapidly when the current reaches 1.6 mA. For higher current the IVC turns linear; cf. the inset in Fig. 3(a). The strong increase of the differential resistance above 1.6 mA is likely to be caused by the NbSe₂ electrodes getting resistive. When the bias current is reduced to values below I_c , a distinct

hysteresis can be observed, until the bias current is reduced to the retrapping current $I_r \approx 0.46$ mA. The overall IVC is very similar to the curves reported in Ref. [21] and basically has the shape of a superconductor-insulator-superconductor (SIS) tunnel junction, with the gap feature appearing at $2\Delta/e \approx 1.64$ mV. For our junctions the subgap resistivity is relatively low. Near the return current a subgap feature occurs at a voltage near $2\Delta/(3e) \approx 0.55$ mV. It may be either related to Andreev-reflectionlike processes or to the excitation of an electromagnetic cavity resonance. Subharmonic gap structures can indeed occur even in SIS tunnel junctions [23]. The frequency of cavity resonances depends both on the shape of the junction (irregular in our case) and on the mode velocity which, in the limit of very thin electrode thicknesses, is proportional to the ratio of the London penetration depth and the electrode thickness [24,25]. All these quantities come with high inaccuracy in our case, but a resonance frequency of about 260 GHz, required to explain the feature is within the error bars.

The critical current density of junction A is 1.1 kA/cm² and the linearized junction resistance near I_c is $R = 1.48 \Omega$, leading to a resistance times area product of $1.5 \times 10^{-6} \Omega \text{ cm}^2$. These numbers are roughly an order of magnitude lower than the ones reported in Ref. [21], indicating that for our junction the transparency of the vdW barrier is somewhat lower. Let us compare the experimental IVC to numerical simulation based on the standard resistively and capacitively shunted junction (RCSJ) model [26,27], in order to get a rough idea about the characteristic frequency scales of the junction. The simulated IVC is shown by the black line in Fig. 3(a). To reproduce the hysteresis (the ratio I_r/I_c) a Stewart-McCumber parameter $\beta_c = 2\pi I_c R^2 C / \Phi_0 = 9$ is required, where C denotes the junction capacitance and Φ_0 is the flux quantum. With $I_c = 1.1$ mA and $R = 1.48 \Omega$ one finds $C = 1.2$ pF. Taking the dielectric permittivity of vacuum, one obtains a distance d between the two NbSe₂ flakes of 0.75 nm, which is close to the vdW gap of 0.6 nm in pristine single crystals. The Stewart-McCumber parameter can also be defined as $\beta_c = (f_c/f_{pl})^2$, where $f_c = I_c R / \Phi_0$ is the characteristic frequency and $f_{pl} = (2\pi \Phi_0 C / I_c)^{-1/2}$ is the Josephson plasma frequency. We then find that f_c and f_{pl} are about 785 and 260 GHz, respectively. Below, in the context of IVCs obtained in external microwave fields, we will see that Joule heating affects the transport characteristics of junction A at 2.95 K data. The corresponding simulations, which combine the RCSJ model with heat-diffusion equations, require a slight reduction of β_c from 9 to 8, which lowers our estimate of C to about 1.1 pF and changes the estimate of f_{pl} to about 245 GHz. The overall IVC obtained in these calculations is nearly indistinguishable from the RCSJ curve shown in Fig. 3(a) and we thus omit it here. Finally, the value of f_{pl} can also be estimated from the voltage jump from the resistive state to the zero-voltage state which occurs at roughly $\Phi_0 f_{pl}$, yielding a value of 242 GHz consistent with the above estimates.

Figure 3(b) shows the IVC of junction A at an elevated bath temperature, $T = 4.0$ K. The critical current is reduced and I_r/I_c is increased compared to the 2.95 K data, and we observe additional voltage jumps and hysteric regions at higher currents and voltages. The additional voltage jumps strongly indicate that regions in the NbSe₂ flakes get resistive.

The observed hysteresis associated with these jumps is most likely of thermal origin.

Figure 4(a) shows, both for positive and negative bias currents, the critical current and the return current of junction A as a function of temperature. The solid lines give the temperature dependence of the critical current of an SIS junction, according to the Ambegaokar-Baratoff theory [28], $I_c R = (\pi/2e)\Delta \tanh(\Delta/2k_B T)$. The data roughly follow these lines, although the agreement is not perfect. When extrapolating this Ambegaokar-Baratoff curve to zero temperature one obtains a zero-temperature critical current of 1.29 mA, which is 45% higher than the value expected from the Ambegaokar-Baratoff formula using $\Delta(0) = 0.84$ meV and $R = 1.48 \Omega$. For comparison Fig. 4(b) shows the temperature dependence of the critical current and of the return current of junction B for positive bias. For this junction I_c follows the Ambegaokar-Baratoff relation much closer and the zero-temperature value of I_c of 0.265 mA is close to the value expected for $\Delta(0) = 0.84$ meV and $R = 5 \Omega$. Figure 4(c) displays five IVCs for this junction, taken at different temperatures. Like for junction A also the IVCs of junction B are hysteretic at low temperatures, although the switching voltage (at low temperature) for unclear reasons is much smaller than for junction A, i.e., switching occurs in the subgap regime well below the gap voltage. The 3.2 K critical current is 0.2 mA. With a junction area of $175 \mu\text{m}^2$ we obtain a critical current density of 115 A/cm^2 , i.e., one order of magnitude less than for junction A. In the IVCs, besides the bump near 0.3 mV on the return branch of the 3.2 K curve, there are pronounced wiggles in particular at temperatures above 4 K. As we will see below, upon microwave irradiation Shapiro steps are observed at the “correct” positions; thus, the bumps and wiggles cannot be associated with the appearance of an additional voltage in the NbSe₂ electrodes. Instead, the features may be related to subharmonic gap structures arising, e.g., from Andreev reflection processes. To compare the 3.2 K IVC with simulations we note that the IVC has a large excess current $I_{\text{ex}} \approx 130 \mu\text{A}$ when extrapolating the high-voltage part of the IVC, having a resistance $R \approx 5 \Omega$, back to zero. In simulations we can take this excess current into account by adding a current term $I_{\text{ex}} \tanh(\alpha u)$ to the RCSJ equations, as proposed in Ref. [29] (RCSJ+EX model). Here, $u = U/I_c R$ is the normalized momentary voltage across the junction. At low voltages the term basically constitutes an excess conductance $\alpha I_{\text{ex}}/I_c R$. More details are given in Appendix B. We find reasonable agreement with the measured IVC by using $\alpha = 3.5$ and $\beta_c = 25$; cf. the dotted line in Fig. 4(c). From β_c and the values of I_c and R we obtain 97 GHz for f_{pl} . From the measured voltage jump from the resistive state back to the zero-voltage state we estimate $f_{\text{pl}} \sim 100$ GHz. Thus, f_{pl} is by a factor of 2.5 lower than for junction A. Since $f_{\text{pl}} \propto j_c^{-1/2}$ this is roughly the expected reduction, provided that the capacitance per unit area—and thus the vdW gap—is the same for both junctions. The same conclusion can be obtained by determining C from $\beta_c = 25$, $I_c = 0.2$ mA, and $R = 5 \Omega$. This yields $C = 1.65$ pF, i.e., an about 10% smaller C/A as for junction A, so C/A is

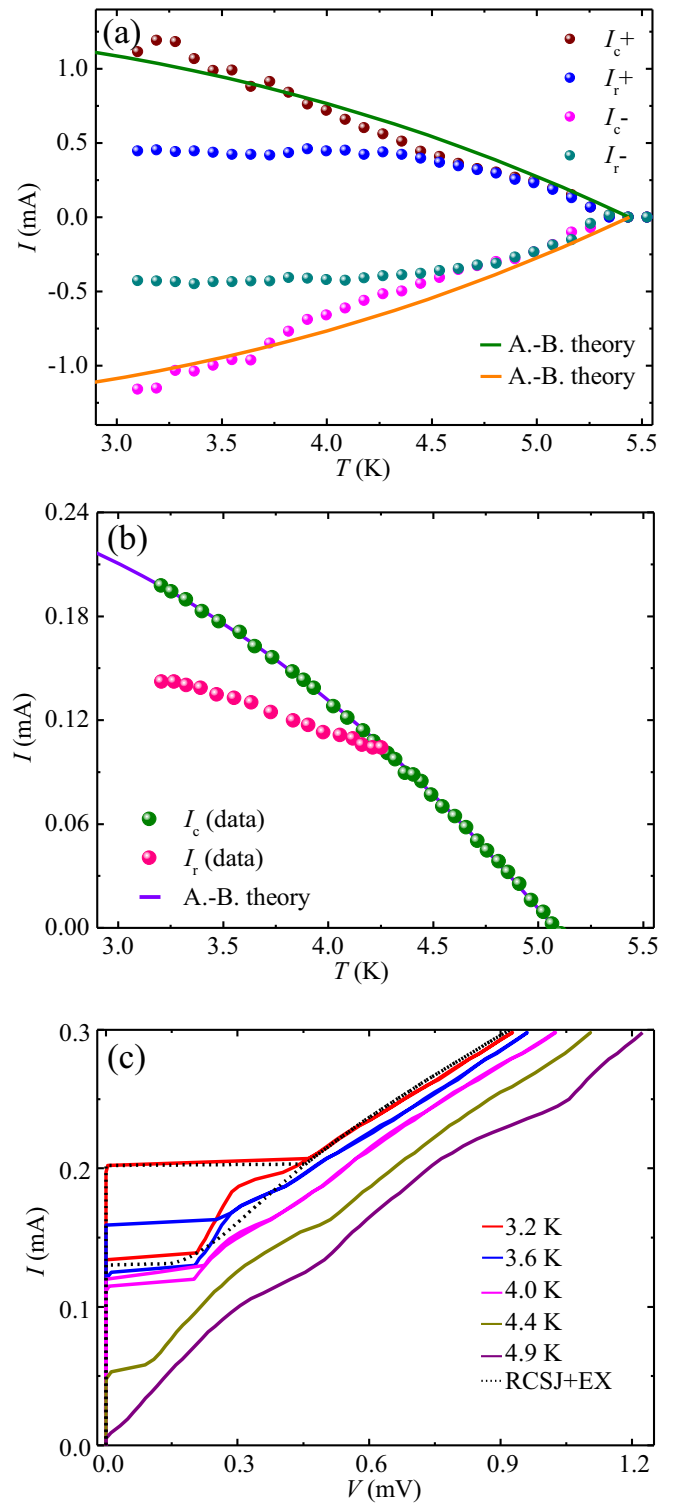


FIG. 4. (a) Junction A: critical current and return current vs temperature, for both polarities of the bias currents. (b) Junction B: critical current and return current vs temperature. Solid lines in the main graphs correspond to the Ambegaokar-Baratoff dependence of $I_c(T)$. (c) IVCs of junction B at five different temperatures. The dotted line is a fit to the 3.2 K IVC using the RCSJ+EX model.

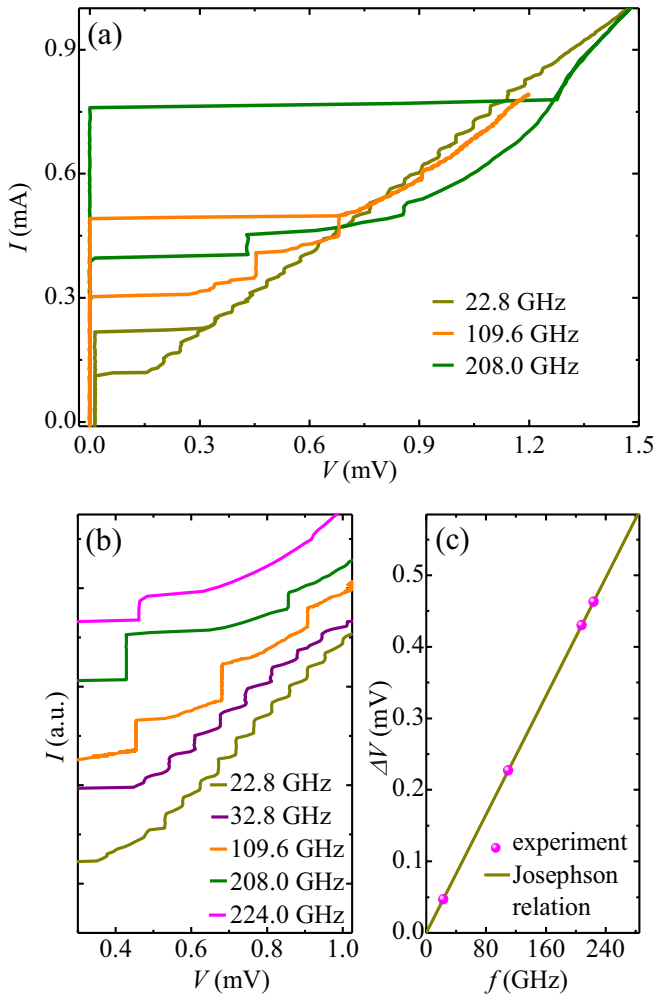


FIG. 5. Junction A at $T = 2.95$ K under microwave irradiation. (a) IVCs for three different frequencies. (b) Zoom of the return branches, with additional 32.8- and 224-GHz data. (c) Voltage spacing ΔV of the Shapiro steps vs microwave frequency. The solid line corresponds to the Josephson relation.

indeed almost the same for both junctions. By contrast, both the critical current density and the resistance area product, being exponentially dependent on the height and thickness of the tunnel barrier, differ by roughly an order of magnitude. This indicates that the tunnel barrier is somewhat different between the two junctions and less transparent for junction B than for junction A.

We briefly mention here that we also attempted to measure $I_c(B)$, i.e., the magnetic field dependence of the critical current. However, even in a moderate field of a few G, far below the expected first minimum in $I_c(B)$, the IVCs became strongly asymmetric with respect to the polarity of the bias current, pointing to trapped flux. We thus cannot give a clear statement on the homogeneity of the critical current density. More details are given in Appendix C.

B. Microwave response

We now turn to the behavior of the two junctions in microwave fields. Figure 5 shows data for junction A, mea-

sured at 2.95 K. The IVCs are shown for $f = 22.8, 109.6,$ and 208 GHz. There are clear Shapiro steps at voltages $V_n = n\Phi_0 f$, with integer n . The Shapiro steps appear on the return branches of the IVCs. A zoom of the return branches is shown in Fig. 5(b), where we also include data for 32.6- and 224-GHz irradiation, and in Fig. 5(c) we plot the voltage spacing ΔV of the Shapiro steps vs the applied frequency. The solid line is given by the Josephson relation $\Delta V = \Phi_0 f$. While the data show that the Josephson relation is fulfilled and point to a sinusoidal current-phase relation, a distinct feature is the fact that the Shapiro steps appear on the return branch of the IVCs in the presence of a hysteresis, even for the lowest applied frequencies. By analyzing the IVCs in the absence of microwaves we have estimated a Josephson plasma frequency of around 245 GHz for junction A. At least in the framework of the RCSJ model one would expect that, for frequencies well below f_{pl} , with increasing microwave power the hysteresis becomes suppressed before stable Shapiro steps appear in the absence of hysteresis. At intermediate values of the microwave power there may chaotic regions in addition. Stable Shapiro steps in the presence of a (thermally caused) hysteresis can, however, occur in high-current density junctions where Joule heating is strong and the electronic temperature on the resistive branches of the IVCs can be well above the bath temperature [30,31]. Such a scenario may also hold for junction A, presumably in combination with capacitive effects.

To be more concrete we plot in Fig. 6(a) 32.8-GHz experimental microwave data for four values of the microwave amplitude $P^{1/2}$ (at the output of the microwave generator) between 1.35 and $5.5 \text{ mW}^{1/2}$, to be compared with the simulated curves shown in Fig. 6(b). The simulation starts from the RCSJ model but takes Joule heating into account by simultaneously solving the one-dimensional heat-diffusion equation, as described in Ref. [32]. In the model, Joule heating increases the junction temperature to a value above the bath temperature, which in turn affects the temperature-dependent junction parameters, i.e., resistance and critical current. More details are given in Appendix B. The simulations shown in Fig. 6(b) are intended to be an illustration and not a fit, because of too many unknown parameters like temperature dependence (and nonlinearities) of the subgap resistance, the junction capacitance, the thermal conductance, and the local (3D) junction geometry. For the simulations we used a temperature-independent junction resistance and a linear temperature dependence of the critical current, with a T_c of 5.2 K. To mention for completeness, the thermal conductance of the junction was set to $K = K_0 T^4$, with $K_0 = 3.5 \text{ nW/K}^5$ at 2.9 K. More importantly, by using $\beta_c = 8$, i.e., somewhat less than for the standard RCSJ simulation shown in Fig. 3(a), the model reproduces the hysteresis (the ratio I_r/I_c in the IVC in the absence of microwaves (black lines in Fig. 6). For the case of $\beta_c = 0$ (not shown) I_r/I_c in the simulated IVC is about 75% larger than for the case of $\beta_c = 8$, i.e., capacitive effects dominate the hysteresis. However, in the absence of heating the hysteresis in the IVC has disappeared already at a microwave power of 1.35 mW ($I_{ac}/I_c = 0.15$) while it persists when we include heating. For increasing microwave power, Shapiro steps appear on the return curve of the simulated IVCs, similarly to the experimental case. In the simulations

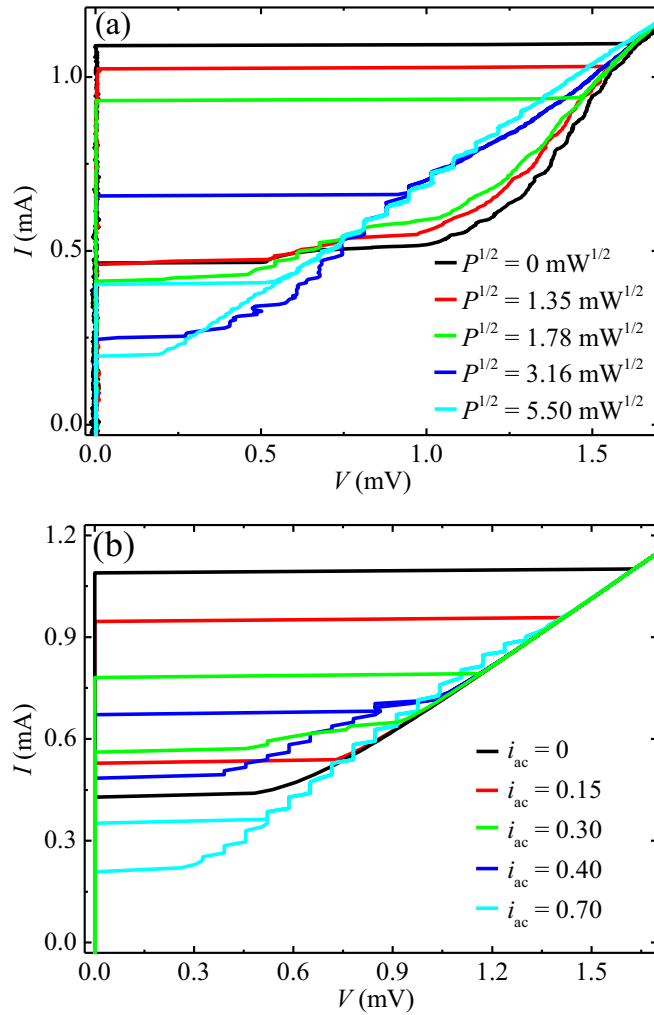


FIG. 6. (a) IVCs for junction A at $T = 2.95$ K in a 32.8-GHz microwave field for different values of the microwave amplitude. (b) Simulated IVCs using an RCSJ model combined with heat-diffusion equations, for different values of the normalized microwave amplitude $i_{ac} = I_{ac}/I_c$. For details, see text.

the junction temperature reaches T_c at about 1.3 mA, while the switch-back in the return curve occurs at a junction temperature of about 3.5 K, i.e., well below T_c .

In Fig. 7 we show microwave data for junction B for frequencies of (a) 214.4 and (b) 30 GHz for different values of the applied microwave power. We estimated the Josephson plasma frequency to be around 100 GHz, i.e., the higher applied microwave frequency is well above f_{pl} while the lower one is about a factor of 3 below f_{pl} .

At $f = 214.4$ GHz the hysteresis in the IVC has disappeared even at the lowest microwave power, and the first Shapiro step is visible for microwave powers between 1.0 and 1.22 $\text{mW}^{1/2}$. For $f = 30$ GHz one observes the reappearance of the hysteresis at intermediate values (0.94 $\text{mW}^{1/2}$) of the microwave power and the appearance of chaotic regions with a negative differential resistance. In particular, at high values of the microwave power the IVC is more regular with the appearance of a large number of integer Shapiro steps. This can be seen in more detail in Fig. 8(a), where we plot the

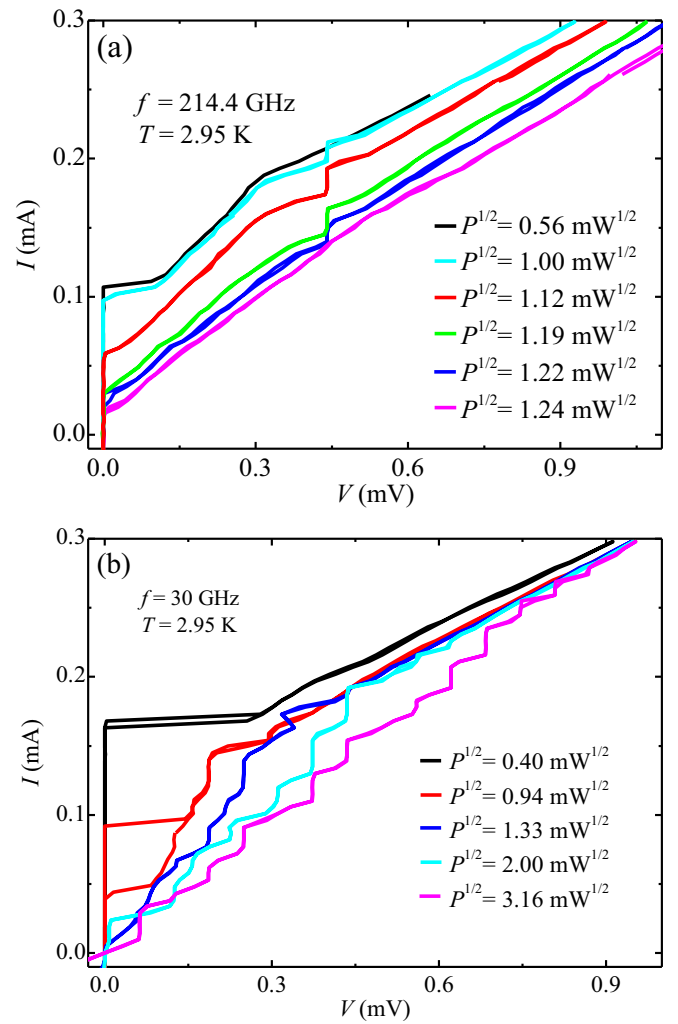


FIG. 7. IVCs of junction B under microwave irradiation at (a) $f = 214.5$ GHz and (b) $f = 30$ GHz. The bath temperature is 2.95 K.

differential resistance of junction B (color scale) as a function of bias current and microwave amplitude, for a microwave frequency of 30 GHz. Overall, compared to junction A, the behavior of the IVCs of junction B in microwave fields is more “conventional,” in the sense that we partially have chaotic regions for the lower microwave frequencies at intermediate values of the microwave power, while stable Shapiro steps appear in the absence of a hysteresis in the IVC. For the higher frequency no chaotic regions are observed. Figure 8(b) shows the results of simulations using the RCSJ+EX model. The agreement with experiment is not perfect—in particular, chaotic regions are observed over a wide range of the induced microwave current—but may still underline our statement that for junction B Joule heating is less important than for junction A. The different importance of heating may also be seen by looking at a characteristic power $P_c = I_c^2 R$. For junction A, P_c is about 1.8 μW while for junction B it is only about 200 nW.

Finally, we briefly address the question, if the Shapiro steps are generated in the NbSe₂ flakes rather than at the vdW interface. Microwave-induced steps in pure NbSe₂ have indeed been observed [33]. However, in this case the relation between

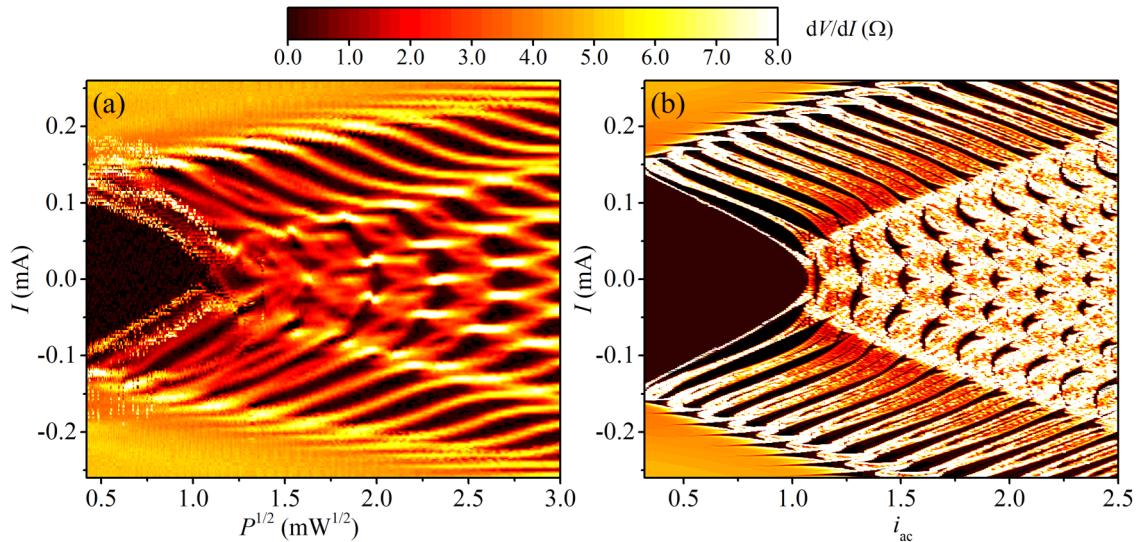


FIG. 8. (a) Differential resistance of junction B (color scale) as a function of bias current and microwave amplitude $P^{1/2}$. The microwave frequency is $f = 30$ GHz and the bath temperature is 2.95 K. (b) Simulated dependence of the differential resistance in a 30-GHz microwave field as a function of bias current and the normalized microwave current $i_{ac} = I_{ac}/I_c$. Simulations are performed within the RCSJ +EX model.

microwave-induced steps and irradiation power is much more complex and different from the typical RCSJ-type junction behavior, in contrast to our observations. We can thus rule out this possibility.

IV. SUMMARY AND CONCLUSIONS

To summarize: The focus of the present study was an investigation of the microwave response of vdW Josephson junctions formed at the interface between two NbSe₂ crystal flakes. We have fabricated nine of these junctions using a dry-transfer method. We found a strong sample-to-sample variation of the current-voltage characteristics, ranging from complete overheating in the resistive state via nonhysteretic curves indicative of resistive shunting to tunnelinglike characteristics. Overheating can happen when the bias current exceeds the in-plane critical current of the NbSe₂ flakes. Shunted behavior may be caused by currents flowing in plane rather than through the vertical vdW contact area. Some variations may also be caused by contaminants on the vdW interface or by the relative orientation of the crystal axes of the two flakes, which we did not control in our experiments.

In the main text we presented and discussed in detail the electric transport properties of two tunnelinglike junctions that neither exhibited pure overheating nor heavy shunting properties. The two junctions differ in critical current density j_c and in the resistance area product by one order of magnitude.

We first precharacterized the two junctions via DC transport experiments. The IVCs of both junctions are hysteretic at low temperatures. The IVC of the high- j_c junction exhibits a clear gap feature near $2\Delta/e \approx 1.64$ mV. From an analysis based on the RCSJ model we deduce a thickness of the tunnel barrier of about 0.75 nm, which is close to the vdW gap of pristine NbSe₂ crystals. For the low- j_c junction the gap voltage could not be reached, but the IVC exhibits various subgap features, and from the analysis of the hysteresis in the

IVC we obtain the same vdW gap of 0.75 nm as for the high- j_c junction. In addition, the temperature dependence of the junction can be well described by the Ambegaokar-Baratoff theory, with a zero temperature gap of 0.84 meV.

For our studies of the AC Josephson effect we irradiated the junctions with frequencies between 22 and 224 GHz. Both junctions show clear integer Shapiro steps up to the highest frequencies. For the high- j_c junction, some features, like the appearance of hysteresis in the IVC in the presence of stable Shapiro steps, indicate that Joule heating is relevant. By contrast, the low- j_c junction at least qualitatively follows the behavior expected from RCSJ-type models, once an excess current is taken into account.

While apparently there is still room for improvement in terms of reproducibility, our results may demonstrate that NbSe₂ vdW Josephson junctions are suited for high-frequency applications at least in principle. However, nonequilibrium phenomena are important and need to be considered in order to understand this type of junction. Another issue regards the thickness of the NbSe₂ flakes, which for the junctions discussed in the main text was 30 nm or larger. In some of our experiments the (in-plane) critical current of the flakes was exceeded and the issue will become more severe if one were to reduce the thickness to only a few or even a single unit cell, posing restrictions on the size of vdW Josephson junctions.

ACKNOWLEDGMENTS

We gratefully acknowledge financial support by the National Natural Science Foundation of China (Grants No. 61727805, No. 11961141002, No. 61521001, and No. 61771235), the National Key R&D Program of China (Grant No. 2018YFA0209002), Jiangsu Key Laboratory of Advanced Techniques for Manipulating Electromagnetic Waves, and the EU-FP6-COST Action No. CA16218.

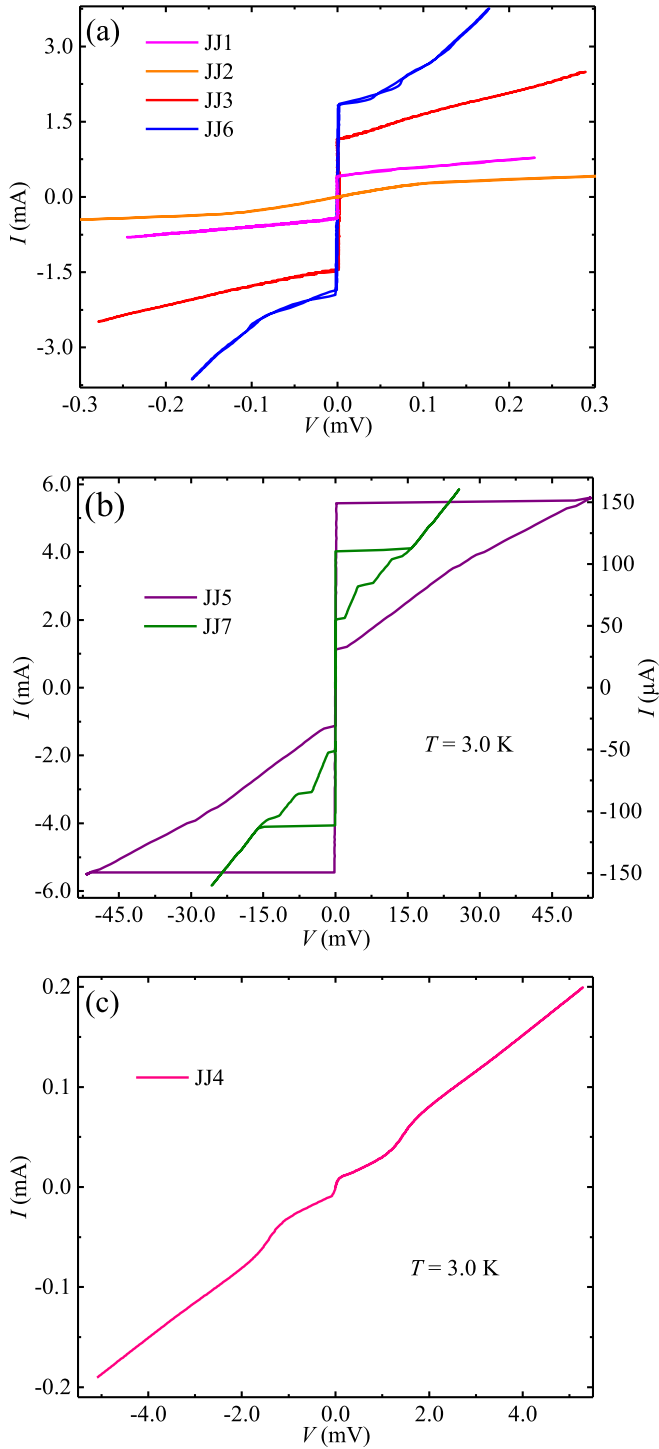


FIG. 9. IVCs, measured at 3 K, for the seven devices not discussed in the main text. Due to very different current and voltage ranges, IVCs for junctions 1, 2, 3, and 6 are included in (a), IVCs for junctions 5 and 7 are shown in (b), and the IVC for junction 4 is displayed in (c).

APPENDIX A: ADDITIONAL DATA FOR JUNCTIONS NOT DISCUSSED IN THE MAIN TEXT

Figure 9 shows IVCs, as measured around 3.0 K for the seven devices not discussed in the main text. For all nine devices electrical and geometrical parameters are listed in

Table I. Quantities listed are the critical current I_c , the normal state resistance R_n , the characteristic voltage V_c , the junction area A , the critical current density j_c , and the product of junction resistance and area RA . We also added a “Comment” column to give a qualitative assessment of the main junction properties. There is a large sample-to-sample variation, which, however is not too different from the devices reported in [Refs. [21,22]].

Figure 9(a) displays IVCs for junctions JJ1, JJ2, JJ3, and JJ6. These junctions have a nonhysteretic IVC for not too large currents and voltages. The IVC of JJ6 is RSJ-like while the IVCs of JJ1 and JJ3 exhibit a significant excess current reminiscent of SNS-type junctions. The critical current densities range from 480 to 1800 A/cm², and the RA products range from 0.063 to 1.7 $\mu\Omega$ cm². For JJ2 there is a finite resistance already at zero bias but one notes that there is a kink near 0.27 mA. For this junction we cannot rule out that we picked up a serial resistance in our measurement scheme. If one would subtract this resistance one would obtain an IVC which looks similar to the IVC of JJ1.

The IVCs of junctions JJ5 and JJ6, exhibiting clear signatures of overheating, are shown in 9(b). Note that in the resistive state the voltage drop is much larger than the gap voltage, indicating that also the NbSe₂ electrodes are driven resistive. The IVC of junction JJ4 is displayed in Fig. 9(c). Here we see signatures of a gap voltage but the junction critical current is highly suppressed.

APPENDIX B: SIMULATION DETAILS

The extended RCSJ model (RCSJ+EX model) introduced in Ref. [29] takes the effect of an excess current into account as an additional term in the RCSJ equations. The RCSJ+EX model can be written in a normalized form as:

$$i + i_{ac} \sin(f\tau) = \beta_c \frac{d^2\varphi}{d\tau^2} + \frac{d\varphi}{d\tau} + \sin(\varphi) + i_{ex} \tanh\left(\alpha \frac{d\varphi}{d\tau}\right), \quad (\text{B1})$$

where φ is the Josephson phase difference, i is the bias current normalized to I_c , and the time t is normalized as

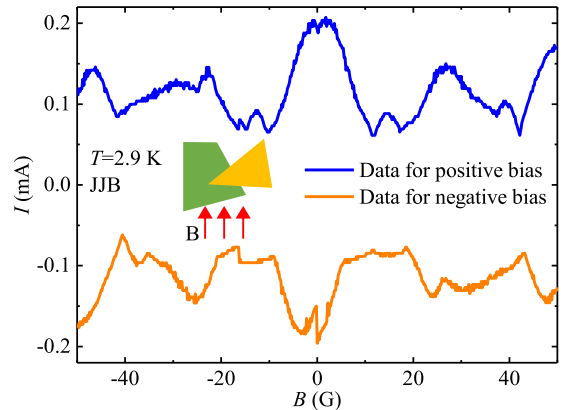


FIG. 10. In-plane magnetic field dependence of the critical current of junction B at 2.9 K. The blue line shows data for positive bias while the orange line is for negative bias. The inset indicates the direction of the applied field.

TABLE I. Electrical and geometrical parameters of all nine devices, including the critical current I_c , the normal state resistance R_n , the characteristic voltage V_c , the junction area A , the critical current density j_c , and the product of junction resistance and area RA . For JJ2 numbers in brackets assume that the kink in the IVC corresponds to the junction critical current.

Junction no.	I_c (mA)	R_n (Ω)	V_c (mV)	A (μm^2)	j_c (A/cm^2)	RA ($\mu\Omega \text{cm}^2$)	Comment
JJ1	0.42	0.71	0.3	100	420	0.71	SNS-like
JJ2	0 (0.27)	1.69	0 (0.46)	100	0 (270)	1.7	Serial resistance
JJ3	1.15	0.22	0.253	100	1150	0.22	SNS-like
JJ4	0.02	25	0.5	30	66.7	7.5	Tunnelinglike, very low I_c
JJ5	5.5	13.89	76.5	100	5500	14.0	Overheated
JJ6	1.8	0.06	0.11	100	1800	0.063	SNS-like
JJ7	0.12	207.8	24.9	100	120	210	Overheated
JJ8 (JJA)	1.1	1.48	1.63	100	1100	1.5	Tunnelinglike
JJ9 (JJB)	0.2	5.2	1.04	175	114.3	8.8	Tunnelinglike

$\tau = 2\pi I_c R t / \Phi_0$. The DC voltage across the junction can be calculated by averaging $d\varphi/d\tau$. In the absence of the last term on the right-hand side of Eq. (B1), one returns to the standard RCSJ model. On the left-hand side, one finds the applied DC current i and an AC current $i_{ac} \sin(f\tau)$, which will be used further to analyze IVCs under microwave irradiation. In this term, the frequency f is measured in units of the characteristic frequency $f_c = I_c R / \Phi_0$. The last term on the right-hand side is related to the excess current, bringing in the two additional parameters i_{ex} and α . For large voltages, the additional term produces a constant current i_{ex} while for low voltages the product $i_{ex}\alpha$ constitutes an (voltage-dependent) excess conductance. In dimensioned units the excess conductance is given by $\alpha I_{ex} / I_c R$. To include heating, like in Ref. [32], we combine Eq. (B1) with the heat-diffusion equation,

$$C_h \dot{T} = P - \int_{T_b}^T K dT, \quad (\text{B2})$$

with the heat capacitance C_h of the junction, the thermal conductance K of the junction to the bath, and the Joule power input $P = U^2/R$. T_b is the bath temperature and T is the actual temperature of the junction. Equation (B1) provides the power input P in Eq. (B2) which in turn delivers the temperature T , to be reimplemented into the temperature-dependent parameters in Eq. (B1). For the simulations we used a temperature-independent junction resistance and a lin-

ear temperature dependence of the critical current, with a T_c of 5.2 K. For the simulations discussed in the main text the thermal conductance of the junction was set to $K = K_0 T^4$, with $K_0 = 3.5 \text{ nW}/\text{K}^5$ at 2.9 K.

APPENDIX C: $I_c(B)$ DATA FOR JUNCTION B

Figure 10 displays the in-plane magnetic field dependence of the critical current for junction B measured at 2.9 K. The inset indicates the (in-plane) magnetic field direction. The blue line shows data for positive bias, while the orange line is for negative bias. The critical current modulations strongly differ from the standard Fraunhofer pattern. One further notes that even at small magnetic fields there are jumps in $I_c(B)$ and strong asymmetries with respect to positive and negative bias. These features strongly indicate flux trapping in the superconducting electrodes, an effect which is well known to spoil $I_c(B)$ patterns even of junctions with a homogeneous critical current density.

Let us nonetheless estimate the magnetic field period where we expect $I_c(B)$ for a well-behaved junction. Using a London penetration depth of 140 nm for NbSe₂ [34], plus the thicknesses of the NbSe₂ electrodes of about 100 and 130 nm, respectively, we find an effective junction thickness [25] of 109 nm, which would correspond to a modulation period of the 15 G for an effective junction width of 15 μm . In Fig. 10, the modulation period of our measurement is about 20 G, which is in reasonable agreement with this estimate.

-
- [1] O. M. Ivanyuta, O. V. Prokopenko, V. M. Raksha, and A. M. Klushin, Microwave detection using Josephson junction arrays integrated in a resonator, *Phys. Status Solidi C* **2**, 1688 (2005).
- [2] E. Holdengreber, A. G. Moshe, M. Mizrahi, V. Khavkin, S. E. Schacham, and E. Farber, High sensitivity high T_c superconducting Josephson junction antenna for 200 GHz detection, *J. Electromagn Waves Appl.* **33**, 193 (2019).
- [3] R. Barends, J. Kelly, A. Megrant, A. Veitia, D. Sank, E. Jeffrey, T. C. White, J. Mutus, A. G. Fowler, B. Camp-bell, Y. Chen, Z. Chen, B. Chiaro, A. Dunsworth, C. Neill, P. O'Malley, P. Roushan, A. Vainsencher, J. Wenner, A. N. Korotkov, A. N. Cleland, and J. M. Martinis, Superconducting quantum circuits at the surface code threshold for fault tolerance, *Nature (London)* **508**, 500 (2014).
- [4] L. B. Ioffe, V. B. Geshkenbein, M. V. Feigel'man, A. L. Fauchère, and G. Blatter, Environmentally decoupled *sds*-wave Josephson junctions for quantum computing, *Nature (London)* **398**, 679 (1999).
- [5] C. Beck, Axion mass estimates from resonant Josephson junctions, *Phys. Dark Univ.* **7**, 6 (2015).
- [6] M. S. Long, P. Wang, H. H. Fang, and W. D. Hu, Progress, challenges, and opportunities for 2D material based photodetectors, *Adv. Funct. Mater.* **29**, 1 (2019).

- [7] X. Du, I. Skachko, and E. Y. Andrei, Josephson current and multiple Andreev reflections in graphene SNS junctions, *Phys. Rev. B* **77**, 184507 (2008).
- [8] R. Moriya, N. Yabuki, and T. Machida, Superconducting proximity effect in a NbSe₂/graphene van der Waals junction, *Phys. Rev. B* **101**, 054503 (2020).
- [9] I. V. Geim and A. K. Grigorieva, Van der Waals heterostructures, *Nature (London)* **499**, 419 (2013).
- [10] Z. M. Zhang, K. M. Watanabe, T. Taniguchi, and B. J. LeRoy, Local characterization and engineering of proximitized correlated states in graphene/NbSe₂ vertical heterostructures, *Phys. Rev. B* **102**, 085429 (2020).
- [11] J. Li, H. B. Leng, H. L. Fu, K. J. Watanabe, T. Taniguchi, X. Liu, C. X. Liu, and J. Zhu, Superconducting proximity effect in a transparent van der Waals superconductor-metal junction, *Phys. Rev. B* **101**, 195405 (2020).
- [12] E. Zhang, X. Xu, Y. C. Zou, L. F. Ai, X. Dong, C. Huang, P. L. Leng, S. S. Liu, Y. D. Zhang, Z. H. Jia, X. Y. Peng, M. H. Zhao, Y. K. Yang, Z. H. Li, H. W. Guo, S. J. Haigh, N. Nagaosa, J. Shen, and F. X. Xiu, Nonreciprocal superconducting NbSe₂ antenna, *Nat. Commun.* **11**, 5634 (2020).
- [13] B. Guster, C. Rubio Verdú, R. Robles, J. Zaldivar, P. Dreher, M. Pruneda, J. A. SilvaGuillén, D. J. Choi, J. I. Pascual, and M. M. Ugeda, Coexistence of elastic modulations in the charge density wave state of 2H-NbSe₂, *Nano Lett.* **19**, 3027 (2019).
- [14] E. Sohn, X. X. Xi, W. Y. He, S. G. Jiang, and K. F. Mak, An unusual continuous paramagnetic-limited superconducting phase transition in 2D NbSe₂, *Nat. Mater.* **17**, 504 (2018).
- [15] F. Calavalle, P. Dreher, A. P. Surdendran, W. Wan, M. Timpel, R. Verucchi, C. Rogero, T. Bauch, F. Lombardi, F. Casanova, M. V. Nardi, M. M. Ugeda, L. E. Hueso, and M. Gobbi, Tailoring superconductivity in large area single-layer NbSe₂ via self-assembled molecular adlayers, *Nano Lett.* **21**, 136 (2021).
- [16] Y. Xing, K. Zhao, P. J. Shan, F. P. Zheng, Y. W. Zhang, H. L. Fu, Y. Liu, M. L. Tian, C. Y. Xi, H. W. Liu, J. Feng, X. Lin, S. H. Ji, X. Chen, Q. K. Xue, and J. Wang, Ising superconductivity and quantum phase transition in macro-size monolayer NbSe₂, *Nano Lett.* **17**, 6802 (2017).
- [17] J. Li, P. Song, J. P. Zhao, K. Vaklinova, X. X. Zhao, Z. J. Li, Z. Z. Qiu, Z. H. Wang, L. Lin, M. Zhao, T. S. Heng, Y. X. Zuo, W. Jonhson, W. i Yu, X. Hai, P. Lyu, H. M. Xu, H. M. Yang, Ch. Chen, S. J. Pennycook, J. Ding, J. H. Teng, A. H. Castro Neto, K. S. Novoselov, and J. Lu, Printable two-dimensional superconducting monolayers, *Nat. Mater.* **20**, 181 (2021).
- [18] C. Chen, P. Das, E. Aytan, W. M. Zhou, J. Horowitz, B. Satpati, A. A. Balandin, R. K. Lake, and P. Wei, Strain controlled superconductivity in few-layer NbSe₂, *ACS Appl. Mater. Interfaces* **12**, 38744 (2020).
- [19] J. Y. Lee, M. Kim, K. J. Watanabe, T. Taniguchi, G. H. Lee, and H. J. Lee, Planar graphene Josephson coupling via van der Waals superconducting contacts, *Curr. Appl. Phys.* **19**, 251 (2019).
- [20] M. Kim, G. H. Park, J. Y. Lee, J. H. Lee, J. Park, H. Lee, G. H. Lee, and H. J. Lee, Strong proximity Josephson coupling in vertically stacked NbSe₂-graphene-NbSe₂ van der Waals junctions, *Nano Lett.* **17**, 6125 (2017).
- [21] N. Yabuki, R. Moriya, M. Arai, Y. Sata, S. Morikawa, S. Masubuchi, and T. Machida, Supercurrent in van der Waals Josephson junction, *Nat. Commun.* **7**, 3015 (2016).
- [22] L. S. Farrar, A. Nevill, Z. J. Lim, G. Balakrishnan, S. Dale, and S. J. Bending, Superconducting quantum interference in twisted van der Waals heterostructures, *Nano Lett.* **21**, 6725 (2021).
- [23] E. N. Bratus', V. S. Shumeiko, and G. Wendin, Theory of subharmonic gap structure in superconducting mesoscopic tunnel contacts, *Phys. Rev. Lett.* **74**, 2110 (1995).
- [24] J. C. Swihart, Field solution for a thin film superconducting transmission line, *J Appl. Physics* **32**, 461 (1961).
- [25] M. Wehnacht, Influence of film thickness on D. C. Josephson current, *Phys. Status Solidi* **32**, K169 (1969).
- [26] W. C. Stewart, Current-voltage characteristics of Josephson junctions, *Appl. Phys. Lett.* **12**, 277 (1968).
- [27] D. E. McCumber, Effect of ac impedance on dc voltage-current characteristics of superconductor weak link junctions, *J. Appl. Phys.* **39**, 3113 (1968).
- [28] Y. Ota, N. Nakai, H. Nakamura, M. Machida, D. Inotani, Y. Ohashi, T. Koyama, and H. Matsumoto, Ambegaokar-Baratoff relations for Josephson critical current in heterojunctions with multi-gap superconductors, *Phys. Rev. B* **81**, 214511 (2010).
- [29] P. Baars, A. Richter, and U. Merkt, Temperature and power dependence of Shapiro and Fiske step widths in Nb/InAs/Nb Josephson junctions, *Phys. Rev. B* **67**, 224501 (2003).
- [30] A. D. Cecco, L. K. Calvez, B. Sacépé, C. B. Winkelmann, and H. Courtois, Interplay between electron overheating and ac Josephson effect, *Phys. Rev. B* **93**, 180505(R) (2016).
- [31] C. D. Shelly, P. See, I. Rungger, and J. M. Williams, Existence of Shapiro steps in the dissipative regime in superconducting weak links, *Phys. Rev. Appl.* **13**, 024070 (2020).
- [32] W. Chen, Z. Y. Xu, W. H. Tian, Y. Y. Lv, M. Yu, X. J. Zhou, X. C. Tu, J. B. Wu, J. Li, S. L. Li, B. B. Jin, W. W. Xu, D. Koelle, R. Kleiner, H. Wang, and P. H. Wu, High-quality in situ fabricated Nb Josephson junctions with black phosphorus barriers, *Supercond. Sci. Technol.* **32**, 115005 (2019).
- [33] S. Tran, J. Sell, and J. R. Williams, Dynamical Josephson effects in NbSe₂, *Phys. Rev. Research* **2**, 043204 (2020).
- [34] J. D. Fletcher, A. Carrington, P. Diener, P. Rodière, J. P. Brison, R. Prozorov, T. Olheiser, and R. W. Giannetta, Penetration Depth Study of Superconducting Gap Structure of 2H-NbSe₂, *Phys. Rev. Lett.* **98**, 057003 (2007).